A digital mapping application for quantifying and displaying air temperatures at high spatiotemporal resolutions in near real-time across Australia

Mathew Webb [1], Budiman Minasny [1]

[1] School of Life and Environmental Sciences & Sydney Institute of Agriculture, The University of Sydney, Eveleigh, NSW, Australia

Corresponding Author:
Mathew Webb [1]
167 Westbury Rd, Prospect, TAS, 7250, Australia
Email address: mathew.webb@dpipwe.tas.gov.au

14 **Abstract**

15   Surface air temperature (T_a) required for real-time environmental modelling applications should
16   be spatially quantified to capture the nuances of local-scale climates. This study created near
17   real-time air temperature maps at a high spatial resolution across Australia. This mapping is
18   achieved using the thin plate spline (TPS) interpolation in concert with a digital elevation model
19   and 'live' recordings garnered from 534 telemetered Australian Bureau of Meteorology (BoM)
20   automatic weather station (AWS) sites. The interpolation was assessed using cross-validation
21   analysis in a 1-year period using 30-minute interval observation. This was then applied to a fully
22   automated mapping system - based in the R programming language - to produce near real-time
23   maps at sub-hourly intervals. The cross-validation analysis revealed broad similarities across the
24   seasons with mean-absolute error ranging from 1.2°C (autumn and summer) to 1.3°C (winter and
25   spring), and corresponding root-mean-square error in the range 1.6°C to 1.7°C. The R^2 and
26   concordance correlation coefficient (P_c) values were also above 0.8 in each season indicating
27   predictions were strongly correlated to the validation data. On an hourly basis, errors tended to
28   be highest during the late afternoons in spring and summer from 3 pm to 6 pm (AEST),
29   particularly for the coastal areas of Western Australia. The mapping system was trialed over a
30   21-day period from 1 June 2020 to 21 June 2020 with majority of maps completed within 28-
31   minutes of AWS site observations being recorded. All outputs were displayed in a web mapping
32   application to exemplify a real-time application of the outputs. This study found that the methods
33   employed would be highly suited for similar applications requiring real-time processing and
34   delivery of climate data at high spatiotemporal resolutions across a considerably large land mass.

Introduction

A timely and accurate source of air temperature (T_a) data is essential for a wide variety of environmental modelling applications requiring real-time monitoring of environmental change (Lazzarini et al. 2014). This is often gleaned from a network of in-situ telemetered meteorological weather stations that are streamed over the internet (Williams et al. 2011). However, datasets of this nature tend to be relevant for a single geographic location that fail to accurately account for the spatial variability between sites that can vary markedly over short distances (Webb et al. 2016). For applications that rely on location-specific data, observations are often harvested from stations situated kilometers away from their location of interest, resulting in that data not being truly representative of the desired location (Jeffrey et al. 2001; Liu et al. 2018b). Thus, T_a can vary considerably over space and time, often attributed to the effects of topographic, coastal and latitudinal factors (Hutchinson 1991; Jarvis & Stuart 2001a; Wang et al. 2011), cloud cover (Xue et al. 2019), radiative effects from aerosols (Li et al. 2017; Mitchell et al. 1995) and diurnal variation (Liu et al. 2018a). As such, T_a for the purpose of input to real-time modelling applications need to be spatially quantified to dynamically account for these interactions but also at an appropriate spatial and temporal resolution to account for the subtle nuances of local-scale climates.

There has been a plethora of research aimed at interpolating surface air temperature at various spatiotemporal scales (Hutchinson 1991; Jarvis & Stuart 2001b; Jeffrey et al. 2001; Jones et al. 2009; Xu et al. 2018). This is in addition to surface temperature estimated from satellite data (Mao et al. 2017; Sobrino et al. 2020). Or from regional reanalysis of global circulation models at high spatiotemporal resolutions (Bollmeyer et al. 2015; Su et al. 2019). Despite this, their application to real-time monitoring of climate have been limited, or insufficient for local-scale monitoring purposes. For example, a modelling system based on remote sensing data coupled with in-situ meteorological recordings was able to produce air temperature maps in near real-time across the United Arab Emirates (Lazzarini et al. 2014). However, the spatial resolution of ~3km was limited in accounting for lapse rates in highly variable topography, despite the system capable of delivering outputs at very high temporal resolution (every 15-minutes). Similarly, a near real-time drought monitoring tool developed for South Asia (Aadhar & Mishra 2017), capable of producing daily minimum and maximum temperatures at a spatial resolution of 0.05° (~5km), would also require further adaptation for high resolution monitoring. This is in addition to a similar system currently used in Australia, where daily minimum (Tmin) and maximum (Tmax) temperatures are produced from Australian Bureau of Meteorology (BoM) weather station sites using thin plate smoothing spline (TPS) interpolation to deliver daily products at 0.05° (~5km) grid resolution (Jeffrey et al. 2001; Jones et al. 2009). While both datasets are useful for broad-scale analysis requiring up-to-date daily records, they still lacked the resolution for sub-daily real-time monitoring at the local-scale.

74 Recently, a near-real time mapping system was developed to produce air temperature maps at
75 high spatiotemporal resolutions across the state of Tasmania, Australia (Webb et al. 2020). This
76 used a combination of regression trees (RT) and TPS interpolation and capable of consistently
77 producing maps at a spatial resolution of 80m at 1-hourly time steps. Evaluation of the system
78 showed that the TPS method was highly suited to real-time application due to the speed and
79 relative accuracy of the outputs produced. For example, assessment of the TPS interpolation
80 showed root mean square errors were consistently under 1.5°C, in addition to only requiring 2-
81 minutes processing time to produce each map product. In this context, the application would be
82 suited to the estimation of T_a across a much larger geographic space at a similar spatiotemporal
83 resolution. As such, there is also an opportunity to apply this approach on a digital platform for
84 real-time access for end-users.
85
86 The objective of this study was to apply and extend the methods in Webb et al. (2020) for
87 production of T_a maps across continental Australia. TPS interpolation is used to produce T_a maps
88 at sub-hourly intervals (every 30-minutes) based on recordings garnered directly from BoM
89 automatic weather station (AWS) sites. The resulting maps are presented digitally at a spatial
90 resolution of 286m, appropriate for local-scale monitoring purposes. The methods for prediction
91 accuracy are evaluated using historic hourly T_a data captured over a 1-year period, in addition to
92 assessing the efficacy of the system for real-time application and subsequent display of outputs
93 in a purpose-built web mapping application.
94

Materials & Methods

95

Approach

96
97 The present study consisted of 2 parts. Firstly, evaluation of the TPS methodology using cross-
98 validation; and secondly, application of the methodology for operational real-time mapping of T_a
99 (Fig. 1). For the evaluation purpose of the study, a historical dataset of 30-minute interval T_a
100 recordings was garnered from BoM automatic weather station (AWS) sites for the 1-year period
101 1 March 2019 to 29 February 2020. This data was used in a leave-one-out cross-validation
102 exercise to assess the prediction performance of the TPS interpolation method. For the
103 application of the methodology for operational real-time mapping, this was tested over a 21-day
104 period from 1 June 2020 to 21 June 2020. For this purpose, a fully automated mapping system
105 was developed using R programming language (R Development Core Team 2015). Processing
106 performance of this mapping system was evaluated for computational efficiency by analyzing
107 each subsequent spatial output (i.e. the time to taken to produce each T_a map) and therefore
108 assessed for real-time application. Maps produced from the interpolation process are
109 immediately displayed in a web map application.
110

Air temperature (T_a) data

111
112 Air temperature (T_a) data recorded by automatic weather stations (AWS) from the Bureau of
113 Meteorology (BoM) and capable of providing real-time access at 30-minute intervals were

114 considered for primary use in this study (Fig. 2). For evaluating the accuracy of the model, a
115 requirement was set, where each station used for the real-time application should have historic
116 recordings for the previous year, specifically from 1 March 2019 to 29 February 2020. These
117 historical data were used for cross-validation analysis. It should be noted that not all AWS sites
118 had data available for the entire evaluation period. Thus, AWS sites that had least 15 days of
119 recordings – consisting of 30-minute interval recordings in each season - was considered for the
120 evaluation process. AWS sites that did not meet this criterion were discarded from the analysis
121 (192 in total). Thus, the screening process resulted in 534 AWS sites corresponding to a possible
122 17567 recording observations in the evaluation period and relevant to each AWS. It should be
123 noted that AWS air temperature observations are recorded using a resistance temperature
124 detector placed within a Stevenson weather screen at 1.2 m above ground (Bureau of
125 Meteorology 2018). All AWS recordings are telemetered into the BoM climate database and
126 publicly accessible via URL (http://www.bom.gov.au/tas/observations/). These are typically
127 displayed at 30-minute intervals. However, due to telemetry and processing delays, readings tend
128 to lag the true observation time of approximately 10- to 20-minutes.
129
130 **Interpolating T_a using thin plate smoothing splines (TPS)**
131 T_a values garnered from the BoM AWS sites were interpolated on a 30-minute interval basis
132 using thin plate smoothing splines. This was performed to form TPS predictions in the evaluation
133 period (1 March 2019 to 29 February 2020) as well as for application to real-time mapping. Its
134 application involves a trivariate approach whereby latitude, longitude, and elevation variables are
135 used as independent variables, as per Jeffrey et al. (2001). The independent variables of latitude
136 and longitude are used for the partial spline component to account for spatial variation, whereas
137 elevation is combined to account for the temperature lapse rates. The spline component of the
138 algorithm is optimised by minimising the generalized cross validation error from the residual
139 sum of squares (Hutchinson 1991). In this study, the *Fields* statistical package (Nychka et al.
140 2017) was used to implement the TPS algorithm in R software (R Development Core Team
141 2015). To guide the mapping of T_a, the 9-second Digital Elevation Model (DEM) was used
142 (Hutchinson et al. 2008). This was reprojected to Geocentric Datum of Australia 94, Geoscience
143 Australia Lambert projection; and resampled to a spatial resolution of 286 m (roughly equivalent
144 to the spatial resolution of original 9-second DEM). The geographical coordinates of the AWS
145 site locations were then spatially intersected with the newly resampled DEM. This operation
146 provided a consistent template to routinely form TPS models using the AWS observations as
147 data points to the algorithm (on a 30-minute basis). Thus, T_a predictions generated by each TPS
148 model were spatially interpolated using the DEM as the z variable, along with the coordinate
149 parameters of the inherent cell properties of the DEM acting as the latitude (x) and longitude (y)
150 variables. This allowed the spline smoothing parameter to be applied continuously across the
151 geographic feature space of the DEM, resulting in a final mapped prediction; saved as GeoTIFF
152 rasters.
153

Evaluating TPS interpolation

The performance of the TPS algorithm was evaluated in the period from 1 March 2019 to 29 February 2020. A leave-one-out cross-validation procedure was employed for each AWS site, similar to the method employed in Webb et al. 2020. Specifically, the training dataset was split into i parts such that i is equal to the number of AWS sites, i.e. 534. For each AWS in i, the ith AWS site was kept for validation (i.e. using actual recordings from the evaluation period), while the remaining dataset, comprising of the remaining BoM recordings was used for TPS modelling to predict T_a at the ith AWS site. This was performed for each 30-minute interval (h) in the evaluation period to produce a set of modelled TPS estimates versus actual AWS recordings at each site. This equated to 17,567 modelled TPS predictions where observed T_a - recorded from each corresponding AWS site - could then be compared. Validation metrics used to assess the modelling accuracy against the T_a recordings, as per Webb et al. 2020, included the mean absolute error (MAE), root-mean-square error (RMSE), coefficient of determination (R^2) and the concordance coefficient. The concordance coefficient (P_c) was used to assess agreement between TPS predictions x; and actual recordings y; that fall on the 45° line through the origin, as defined by Lin (1989):

$$p_c = \frac{2p\sigma_x\sigma_y}{\sigma_x^2 + \sigma_y^2 + (\mu_x - \mu_x)^2}$$

where for μ_x and μ_x represent the means for x and y, respectively, σ_x^2 and σ_y^2 represent the corresponding variances, and p is the correlation coefficient between x and y. A concordance rating close to one indicates strong agreement between predicted and actual T_a pairings that fall on the 45° line through the origin.

Application to real-time monitoring of T_a

The proposed methodology, as advocated by Webb et al. 2020, was adopted in this study for operational real-time monitoring of T_a across continental Australia. However, since the formation of BoM grids and calibration equations were not required in this study, the methodology was retrofitted to consist of two major components. Firstly, the import of 'live' T_a data via the internet from the BoM website, and secondly, the mapping of the observations using TPS interpolation. This was trialled over a 21-day period from 1 June 2020 to 21 June 2020, using real-time BoM observations to drive the system which was fully automated using software R (R Development Core Team 2015). Because new BoM observations are typically available every 30-minutes, individual AWS site observations were downloaded at this frequency from the BoM observations portal as comma delimited text files (e.g. http://www.bom.gov.au/fwo/IDT60801/IDT60801.<*stationIDnumber*>.axf). Thus, the mapping system was programmed to query and import recordings every 30-minutes (bi-hourly) that corresponded to the nearest half-hour at 0- and 30 minutes (past the hour). Because of telemetry and associated processing delays (observation updates varied from station to station), the system was programmed to make queries at 5, 10, 15, 20, 25 and 30 minutes within their 30-minute

193   processing window. In addition, a threshold was set where at least 480 out of the 534 BoM
194   stations (i.e. 90% of total available AWS sites that were used in the evaluation analysis) have
195   available observations before the mapping was allowed to commence in their respective
196   processing window. This served to limit the number of missing observations that could otherwise
197   produce significant inaccuracies in the subsequent mapped product. However, if this threshold
198   was not met during the allocated query times, the mapping was still permitted to commence at
199   the 30-minute mark regardless of the number of observations available (this was subsequently
200   recorded). To provide context of the proposed system, the same procedure by Webb et al. (2020)
201   found that most observations tended to be imported at the 15-minute mark (from the nearest
202   observation hour) with corresponding TPS maps completed thereafter at the 17-minute mark.
203   The rationale for this study assumes a similar time frame, albeit at bi-hourly intervals, where
204   observations are imported every 30-minutes (with an import time lag of ~15-minues from the
205   nearest half-hour), followed by T_a mapping thereafter. Note that all AWS recording times in this
206   study were standardised to Australian Eastern Standard Time (AEST).

208   To interpolate the TPS predictions, the processing schema described in Webb et al. 2020 was
209   used. This consisted the Raster package (Hijmans & van Etten 2012) in combination with the
210   *Fields* statistical package (Nychka et al. 2017) using software R (R Development Core Team
211   2015), to map and subsequently visualize the predictions in a continuous manner across
212   Australia. To improve processing speed, the clusterR function within the Raster package was
213   parameterised to host the TPS algorithm, thereby enabling mapping to occur using multi-core
214   processors. In this manner, the mapping system was hosted on a high-end cloud computing
215   Linux platform (Ubuntu 18.04 LTS (Bionic)) constituting 16 virtual CPU cores and 64GB RAM;
216   made available courtesy of the Australian National eResearch Collaboration Tools and
217   Resources project (NeCTAR). Spatial outputs were saved as individual GeoTIFF raster format at
218   a grid cell resolution of 286m, i.e. equivalent to the spatial resolution of the resampled DEM.

Results
Assessment of the TPS interpolation procedure
223   Each of the AWS sites underwent the leave-one-out cross-validation analysis to assess TPS
224   prediction accuracy for T_a in the evaluation period: 1 March 2019 to 29 February 2020. This
225   analysis revealed broad similarities across the seasons with MAE values ranging from 1.2°C
226   (autumn and summer) to 1.3°C (winter and spring), and similarly RMSE ranging from 1.6°C to
227   1.7°C (Table 1). The R^2 and P_c values were above 0.8 indicating that the TPS predictions were
228   strongly correlated to the validation data in addition to being highly associated with the 45° line
229   through the origin (Lin 1989). This assessment also implied that predictions were relatively
230   consistent across the evaluation period and did not vary substantially on a seasonal basis.
231   Moreover, it implied that the TPS interpolation was more suited to predicting T_a in autumn which
232   tended to exhibit superior statistics across all validation measures when compared to the other

233   seasons. This was particularly evident regarding R^2 and P_c, which registered the highest values of
234   0.91 and 0.94, respectively. However, TPS predictions tended to be least accurate in spring and
235   winter which had MAE and RMSE values greater by 0.1°C, when compared to the
236   corresponding MAE and RMSE values in autumn. Interestingly, although spring exhibited
237   comparatively inferior MAE and RMSE values, the R^2 statistics were similar, both registering
238   0.91. This suggests that while errors were comparatively larger in spring, they were still very
239   highly correlated to the validation data. However, it should be noted that the coefficient of
240   determination may have been unrealistically overestimated for spring since the seasonal data
241   signal was not removed prior to analysis, as advocated in Jeffrey et al. (2001).
242
243   When looking at the histogram distribution of the MAE and RMSE it was apparent that spring
244   and winter had a notable proportion of AWS sites that exhibited values above 2°C (Fig. 3). This
245   contributed to the inflated error values shown in Table 1. Specifically, spring and winter both
246   had a total of 42 and 46 AWS sites that registered MAE above 2°C, compared to 22 and 16 AWS
247   sites for summer and autumn, respectively. Similarly, spring and winter also had a large
248   proportion of RMSE values above 2°C with 147 and 134 AWS sites, respectively, compared to
249   95 and 91 AWS sites for summer and autumn, respectively. In regard to R^2 and P_c, winter had a
250   greater proportion of AWS sites that exhibited moderate to weak correlation (≤0.7) with 45 and
251   32 sites, respectively; compared to 37 and 17 in summer, 11 and 10 in spring, and 13 and 8 in
252   autumn. The high proportion of low R^2 values in winter contributed to the lowest R^2 value of
253   0.86, compared to 0.89, 0.91 and 0.91 for summer, autumn and spring, respectively (Table 1).
254
255   When viewing the errors spatially, it was clear that most of the larger interpolation errors
256   transpired in regions where there was a lack of neighbouring AWS sites (Fig. 4). Specifically, the
257   central and western interior parts of Australia tended to exhibit MAE and RMSE values above
258   2°C, compared to the eastern half where temperatures were consistently predicted within 2°C of
259   the actual T_a. Of note was the predominately high errors encountered for the coastal areas of
260   Western Australia (between Geraldton and Port Hedland) during summer and spring where the
261   MAE and RMSE prediction errors regularly exceeded 2.5°C. For example, the Learmonth
262   Airport AWS site (Fig. 2) in spring had MAE and RMSE of 3.4°C and 4.3°C, respectively, in
263   addition to summer with corresponding MAE and RMSE of 3.2°C and 4.2°C, respectively.
264   Outside of this cluster, there were also high MAE and RMSE values for individual AWS sites
265   located at Pirlangimpi Airport (Tiwi Islands, Northern Territory) in spring with 3.6°C and 4.3°C,
266   respectively; Forrest in Western Australia during summer with corresponding MAE and RMSE
267   of 2.9°C and 3.8°C, respectively; and Yampi Sound in the Northern Territory during winter with
268   MAE and RMSE of 3.3°C and 4.3°C, respectively. Furthermore, in winter there was a notable
269   cluster of high MAE values emanating from central Australia through to the coastal fringes of
270   Northern Territory and Western Australia (i.e. Darwin through to Broome) with MAE and
271   RMSE consistently above 2°C.
272

273   In terms of the R^2 and P_c, low values tended to emanate along the coastal regions, particularly for
274   Western Australia, Northern Territory and North Queensland coastal regions and neighbouring
275   islands (Fig. 4). For example, the lowest values were encountered for sites Pirlangimpi Airport,
276   Browse Island and Coconut Island in spring with R^2 of 0.01, 0.1 and 0.1, respectively, and P_c of
277   0.09, 0.25 and 0.23, respectively. Summer also encountered low R^2 of 0.05, 0.05 and 0.31,
278   respectively, with corresponding P_c of 0.18, 0.2 and 0.52. The same sites in winter also had the
279   lowest R^2 of 0.41, 0.01 and 0.14, respectively, along with corresponding P_c of 0.48, 0.08 and
280   0.27.
281
282   When observing MAE (Fig. 5) and RMSE (Fig. 6) over a 24-hour period, it was clear that the
283   high values encountered for the coastal areas of Western Australia in summer and spring tended
284   to occur during afternoons. Specifically, these had MAE and RMSE ranging between 4-6°C for
285   times 3 pm to 6 pm, i.e. 1 pm to 4 pm, Australian Western Standard Time (AWST). Of note was
286   the Learmonth Airport AWS site registering MAE of 6.9°C and RMSE of 7.6°C, peaking at 5
287   pm (3 pm, AWST) in summer (Fig. 7). Similarly, very high error values were encountered for
288   the south-eastern area of Western Australia in spring, notably for the Forrest AWS site at 6 pm,
289   which registered 6.1°C and 6.3°C for MAE and RMSE, respectively. This was in addition to
290   5.3°C and 7°C, respectively, for the same site in summer, along with the Ceduna AWS site
291   (South Australia) at 6 pm, registering high MAE and RMSE values of 5.4°C and 6°C,
292   respectively. During winter the trend for high MAE and RMSE emanating from central Australia
293   and the coastal fringes of Northern Territory and Western Australia tended to occur during early
294   mornings from 3 am to 9 am (1 am to 7 am, AWST), with MAE and RMSE ranging 3-5°C. The
295   AWS sites with the greatest error in these parts were Adele Island and Yampi Sound which both
296   registered a MAE of 6.4°C and RMSE of 6.4°C and 6.7°C, respectively (Fig. 5 & 6). Both sites
297   are located in the northern coastal region of Western Australia (NB: the locations of all
298   aforementioned AWS sites are depicted in Fig. 2).
299
300   Regarding R^2 and P_c, it was revealed that low values <0.5 were mostly evident during late nights
301   and early mornings, particularly during winter and summer (Fig. 8 & 9). This tended to be
302   prevalent throughout the central western interior and the coastal fringes of Western Australia,
303   Northern Territory and North Queensland. Specifically, R^2 and P_c <0.5 tended to occur from
304   midnight through to 6 am, suggesting that the TPS predictions were not highly correlated with
305   the validation data during these times. This occurred despite the RMSE and MAE registering
306   values below 2°C for some sites. For example, the AWS site at Browse Island during summer at
307   12 am registered R^2 and P_c values of 0.04 and 0.2, respectively, while MAE and RMSE was
308   0.9°C and 1.1°C, respectively (Fig. 7). This was also encountered for the Coconut Island AWS
309   during winter mornings, e.g. at 9 am where the R^2 and P_c values registered 0.0 and 0.1,
310   respectively, while the MAE and RMSE was 1.4°C and 1.7°C, respectively. This suggested that
311   while predictions were reasonably accurate, there was little to no correlation with the validation
312   data.

313

Assessment of mapping T_a in near real-time

315 The TPS methodology was applied to mapping T_a in real-time at 30-minute intervals over a 21-
316 day period from 1 June 2020 to 21 June 2020. This exercise resulted in 1007 maps being
317 produced which aligned to the total number of 30-minute processing intervals in the trial period;
318 confirming all possible maps were successfully processed. On analysing the map completion
319 times, the majority of the maps were completed at 28-minutes (Fig. 10). Specifically, 410 and
320 414 maps were produced for their respective 0- and 30-minute processing intervals. This
321 corresponded directly to the AWS import times (Fig. 11), with the same proportion of AWS
322 observations reaching the 480-observation threshold import limit at the 15-minute mark; thereby
323 permitting T_a mapping to commence. Thus, import times that occurred at 15-minutes, equated to
324 resulting maps being completed at 28-minutes from the AWS observation time. From this, it can
325 be deduced that on all occasions the map processing time was 13-minutes, regardless of the
326 interval being processed. It should be noted that on 35 occasions the 480-observation threshold
327 limit was not reached, resulting in maps - that did not meet this criterion - being produced at the
328 30-minute mark. This equated to 14 and 21 maps produced at the 0- and 30-minute processing
329 intervals, respectively.

330

Discussion

332 **Appraisal of the TPS interpolation procedure**

333 On the whole, the TPS interpolation method was a reliable predictor of T_a across Australia with
334 an RMSE of 1.65°C, i.e. when averaged across the seasons (Table 1). When compared to
335 previous studies, this error was similar to Jeffrey et al. (2001) with RMSE of 1.5°C and 1.9°C for
336 daily maximum and minimum temperatures, respectively; and Jones et al. (2009) with
337 corresponding RMSE of 1.2°C and 1.7°C. On a seasonal basis the TPS predictions tended to be
338 least accurate in spring and winter which had MAE and RMSE values larger by 0.1°C compared
339 to the same measures in autumn. When viewing these errors spatially, it was clear that the
340 majority of the larger interpolation errors transpired in the central and western interior parts of
341 Australia. This is unsurprising given the station density in these parts are relatively sparse in
342 addition to large temperature variances which tend to produce inflated errors (Jeffrey et al. 2001;
343 Jones & Trewin 2000). Of note was the predominately high errors encountered for the coastal
344 areas of Western Australia (between Geraldton and Port Hedland) during summer and spring
345 afternoons where prediction errors were regularly above 2.5°C. This was in addition to high
346 MAE values for individual AWS sites located at Forrest in Western Australia and Ceduna in
347 South Australia. Collectively, these regions tend to experience very strong temperature gradients,
348 particularly concerning maximum temperatures, since their proximity between the coast and
349 inland deserts result in local climate regimes being invariably affected by the relatively cool
350 ocean to the west and hot desert interior to the east (Jones et al. 2009). These are increasingly
351 difficult to model with a sparse network of observation sites since these errors tended to be
352 amplified during mid to late afternoons in late spring and summer when the temperature

353 gradients were at their peak. Also, temperatures in these areas vary considerably over short
354 periods leading to a tendency for larger errors (Jones & Trewin 2000).
355
356 Concerning winter, the trend for high MAE and RMSE in central Australia and coastal fringes of
357 Northern Territory and Western Australia tended to occur during early mornings from 3 am to 9
358 am (1 am to 7 am, AWST). As acknowledged previously, the accuracy of the mapping was
359 limited in these regions due to an insufficient network of AWS sites. Also, AWS sites in the
360 coastal fringes tend to have tight climate gradients as a result of local maritime effects (Jones et
361 al. 2009). This possibly contributed to the low R^2 and P_c values encountered in Fig. 4, 8 & 9 -
362 despite some AWS sites exhibiting relatively small MAE and RMSE values, e.g. Browse Island
363 and Coconut Island AWS sites (Fig. 7). Thus, the predictions tended to be highly variable over a
364 narrower prediction range due to the tighter temperature gradient in these climates. Combined
365 with a sparse network of AWS sites, the TPS method was unable to account for this on a sub-
366 hourly timescale. Moreover, the spread of AWS sites in remote coastal locations – e.g. Adele
367 Island, Yampi Sound and Pirlangimpi Airport AWS sites - tend to have considerably larger
368 errors as a result of unique and often complex microclimates, thereby compounding the
369 variability (Jones et al. 2009). It should also be noted that the larger errors for the central interior
370 parts of Australia may also be due to the weaker link between altitude and temperature – for
371 which the TPS algorithm is reliant (Hutchinson 1991). This is because minimum temperatures
372 have a highly variable and complex relationship with topography for which elevation and its
373 association with lapse rates are only one part (Rolland 2003; Trewin 2005). Considering
374 minimum temperatures tend to transpire during early mornings – as encountered for AWS sites
375 in winter (Fig. 5 & 6) – a multivariate approach to modelling might be more appropriate along
376 with a denser network of AWS sites. This approach was conducted by Webb et al. (2020), and
377 showed errors improved during winter when using regression tree interpolation (along with
378 multiple terrain and satellite covariate datasets). However, the substantially longer processing
379 times may not be appropriate for real-time application, negating its ability to produce outputs in a
380 timely manner as required for this study. Similar experiments contrasting TPS, ordinary kriging
381 and inverse distance weighting interpolation found that TPS was more accurate and required few
382 guiding covariates (Jarvis & Stuart 2001b). This justified the selection of the TPS method in the
383 current study, even though kriging can be an equally effective method (Hutchinson 1991).
384 However, kriging requires considerable computational overhead (Jarvis & Stuart 2001b) and
385 therefore, in the context of this study, not ideal for real-time application.
386
387 It should be commented that the cross-validation analysis adopted in this study would likely
388 overestimate the error since predictions were made at locations that have actual data
389 observations. This would be less of a concern for regions where the number of observation points
390 is numerous, such as for the majority of land areas in south-east Australia – which tended to have
391 more accurate T_a predictions compared to the western interior. Nevertheless, this exemplifies that
392 the sparse network of AWS sites in central and western coastal areas of Australia was a notable

393   factor contributing to larger interpolation errors. It should be further commented that while the
394   cross-validation analysis was valid using a static dataset, in reality and as exemplified during
395   real-time application, interpolation could only commence when the predefined threshold of 480
396   AWS observations was met. Thus, on most occasions' predictions were based on the minimum
397   allowable number of AWS sites and therefore prone to produce less accurate predictions
398   compared to using an entire dataset. To evaluate this scenario, a K-fold cross validation was
399   implemented (Hastie et al. 2009). Specifically, the training dataset - represented by AWS
400   observations in each 30-minute interval (h) within the evaluation period - was split into K equal
401   parts using random sampling. Where the Kth part was kept for validation and the remaining K-1
402   part were combined for TPS modelling in each fold. In this manner, the predictions produced by
403   the modelling were assessed against the held back validation subset and was repeated K times,
404   such that each K validation subset was used once to assess the K-1 model. In this study, K = 10
405   was specified, representing 90% of the dataset for TPS modelling and 10% for validation in each
406   fold, i.e. equivalent to 480 and 54 AWS sites, respectively.
407
408   The result of the K-fold analysis (Table 2) revealed broad similarities with Table 1. For example,
409   the MAE of 1.2°C, 1.2°C, 1.3°C and 1.3°C, respectively for summer, autumn, winter and spring,
410   and corresponding RMSE of 1.7°C, 1.6°C, 1.7°C and 1.8°C, respectively, deviated by no more
411   than 0.1°C when compared to the equivalent measures in Table 1. This indicated that overall the
412   prediction accuracy did not deteriorate greatly when interpolation was based on the minimum
413   allowable number of AWS sites. It also justified that the 480 AWS threshold adopted in this
414   study was an acceptable limit for the real-time application.
415
416   **Appraisal of mapping T_a in near real-time and application to digital mapping**
417   The TPS interpolation applied in real-time was capable of producing sub-hourly T_a maps
418   typically within 28-minutes of the observation being recorded by the available AWS sites (Fig.
419   10). Specifically, import times were generally reached for the predefined threshold of 480
420   observations at the 15-minute mark (Fig. 11) which was followed by a 13-minute processing lag.
421   In this regard, maps were consistently available within their 30-minute processing window and
422   had a high degree of temporal reliability - with all possible maps produced in the 21-day trial
423   period. The resulting maps were presented on a digital web mapping platform to allow real-time
424   access and interrogation ability of each output. An example of this application can be accessed at
425   URL http://austemperature.live/ (Fig. 12). A GeoServer backend was used to host current outputs
426   to allow geospatial representation and sharing of outputs via a Wep Map Service (Open Source
427   Geospatial Foundation 2019). The maps can be spatially queried to reveal temperatures for the
428   current hour and for the previous 3-hrs (at 30-minute intervals). This is enabled via web
429   application packages *shiny* and *leaflet* (Chang et al. 2019; Cheng et al. 2019) within the R
430   programming environment (R Development Core Team 2015). In this fashion, maps can be
431   spatially interrogated via an on-the-fly 'data drilling' for any geographical location in Australia
432   (via mouse click). A facility to view the cross-validation statistics of each map output is also

433   provided as well as the ability to download each newly created map for use in GIS applications.
434   A potential new feature is to provide an error map for each subsequent map produced (similar to
435   Fig. 5 & 6). This would provide an approximate error measure for regions with limited AWS
436   sites which tended to be high, as encountered in this study. Note that rainfall mapping outputs are
437   also presented in the application, although this should be used with caution due to the
438   preliminary nature of this work.
439

Conclusions

441   The methods described in this study were successful for operational real-time spatial mapping of
442   T_a at high spatiotemporal across Australia. The TPS interpolation method was best suited for
443   mapping T_a during autumn and was comparatively less accurate during winter and spring. In
444   particular, areas, where there was a lack of AWS sites, tended to underperform. These areas
445   included the central and western interior regions of Australia, as well for the north-west coastal
446   areas of Western Australia and parts of the Northern Territory coastline. On a temporal basis, the
447   errors were amplified during the afternoons, particularly around the coastal regions of Western
448   Australia, during spring and summer. In winter, errors tended to be higher in central Australia
449   and the coastal fringes of Northern Territory and Western Australia, from 3 am to 9 am. In terms
450   of applying the TPS method to real-time operational mapping, the mapping system was able to
451   regularly provide spatial outputs within 28-minutes of AWS site observations being recorded. In
452   addition, it also had a high degree of temporal reliability with all maps produced in the 21-day
453   trial period. Outputs were sequentially displayed on purpose-built web mapping application to
454   exemplify real-time application of the outputs. In this regard, the methodology employed in this
455   study would be highly suited for similar applications requiring real-time processing and delivery
456   of climate data at high spatiotemporal resolutions across a large landmass, suitably
457   complimented with a relatively dense network of observation sites.
458

Acknowledgements

460   This research was supported by Tasmanian Partnership for Advanced Computing and by use of
461   the Nectar Research Cloud. The Nectar Research Cloud is a collaborative Australian research
462   platform supported by the National Collaborative Research Infrastructure Strategy (NCRIS).
463

464 **References**

465 Aadhar S, and Mishra V. 2017. High-resolution near real-time drought monitoring in South Asia.
466   *Scientific Data* 4:170145. 10.1038/sdata.2017.145
467 Bollmeyer C, Keller JD, Ohlwein C, Wahl S, Crewell S, Friederichs P, Hense A, Keune J, Kneifel
468   S, Pscheidt I, Redl S, and Steinke S. 2015. Towards a high-resolution regional
469   reanalysis for the European CORDEX domain. *Quarterly Journal of the Royal*
470   *Meteorological Society* 141:1-15. 10.1002/qj.2486
471 Bureau of Meteorology. 2018. Bureau of Meteorology website. (Australian Government).
472   *Available at http://www.bom.gov.au/climate/cdo/about/airtemp-measure.shtml* (accessed
473   11 August.
474 Chang W, Cheng J, Allaire J, Xie Y, and McPherson J. 2019. shiny: Web Application
475   Framework for R. R package version 1.4.0. https://CRAN.R-project.org/package=shiny.
476 Cheng J, Karambelkar B, and Xie Y. 2019. leaflet: Create Interactive Web Maps with the
477   JavaScript 'Leaflet' Library. R package version 2.0.3. https://CRAN.R-
478   project.org/package=leaflet.
479 Hastie T, Tibshirani R, and Friedman J. 2009. *The elements of statistical learning (2nd edition)*:
480   Springer-verlag, New York.
481 Hijmans RJ, and van Etten J. 2012. raster: Geographic analysis and modeling with raster data.
482   R package version 2.0-12. http://CRAN.R-project.org/package=raster.
483 Hutchinson M. 1991. The application of thin plate smoothing splines to continent-wide data
484   assimilation. In: Jasper J, editor. Data Assimilation Systems. Melbourne, Vic, Australia:
485   Bureau of Meteorology. p 104-113.
486 Hutchinson MF, Stein JL, Stein JA, Anderson H, and Tickle PK. 2008. GEODATA 9 second
487   DEM and D8: Digital Elevation Model Version 3 and Flow Direction Grid. Record DEM-
488   9S.v3. Geoscience Australia, Canberra.
489 Jarvis CH, and Stuart N. 2001a. A comparison among strategies for interpolating maximum and
490   minimum daily air temperatures. Part I: The selection of "guiding" topographic and land
491   cover variables. *Journal of Applied Meteorology* 40:1060-1074.
492 Jarvis CH, and Stuart N. 2001b. A comparison among strategies for interpolating maximum and
493   minimum daily air temperatures. Part II: The interaction between number of guiding
494   variables and the type of interpolation method. *Journal of Applied Meteorology* 40:1075-
495   1084.
496 Jeffrey SJ, Carter JO, Moodie KB, and Beswick AR. 2001. Using spatial interpolation to
497   construct a comprehensive archive of Australian climate data. *Environmental Modelling*
498   *& Software* 16:309-330. https://doi.org/10.1016/S1364-8152(01)00008-1
499 Jones DA, and Trewin BC. 2000. On the relationships between the El Niño–Southern Oscillation
500   and Australian land surface temperature. *International journal of climatology* 20:697-719.
501   10.1002/1097-0088(20000615)20:7<697::aid-joc499>3.0.co;2-a
502 Jones DA, Wang W, and Fawcett R. 2009. High-quality spatial climate data-sets for Australia.
503   *Australian Meteorological and Oceanographic Journal* 58:233.
504 Lazzarini M, Marpu PR, Eissa Y, and Ghedira H. 2014. Toward a Near Real-Time Product of Air
505   Temperature Maps from Satellite Data and In Situ Measurements in Arid Environments.
506   *IEEE Journal of Selected Topics in Applied Earth Observations and Remote Sensing*
507   7:3093-3104. 10.1109/JSTARS.2014.2320762
508 Li Z, Guo J, Ding A, Liao H, Liu J, Sun Y, Wang T, Xue H, Zhang H, and Zhu B. 2017. Aerosol
509   and boundary-layer interactions and impact on air quality. *National Science Review*
510   4:810-833. 10.1093/nsr/nwx117
511 Lin LIK. 1989. A Concordance Correlation Coefficient to Evaluate Reproducibility. *Biometrics*
512   45:255-268. 10.2307/2532051

513 Liu L, Guo J, Chen W, Wu R, Wang L, Gong H, Xue W, and Li J. 2018a. Large-Scale Pattern of
514   the Diurnal Temperature Range Changes over East Asia and Australia in Boreal Winter:
515   A Perspective of Atmospheric Circulation. *Journal of Climate* 31:2715-2728. 10.1175/jcli-
516   d-17-0608.1
517 Liu S, Su H, Tian J, and Wang W. 2018b. An analysis of spatial representativeness of air
518   temperature monitoring stations. *Theoretical and Applied Climatology* 132:857-865.
519   10.1007/s00704-017-2133-6
520 Mao KB, Ma Y, Tan XL, Shen XY, Liu G, Li ZL, Chen JM, and Xia L. 2017. Global surface
521   temperature change analysis based on MODIS data in recent twelve years. *Advances in*
522   *Space Research* 59:503-512. https://doi.org/10.1016/j.asr.2016.11.007
523 Mitchell JFB, Davis RA, Ingram WJ, and Senior CA. 1995. On Surface Temperature,
524   Greenhouse Gases, and Aerosols: Models and Observations. *Journal of Climate* 8:2364-
525   2386. 10.1175/1520-0442(1995)008<2364:ostgga>2.0.co;2
526 Nychka D, Furrer R, Paige J, and Sain S. 2017. fields: Tools for spatial data. R package version
527   10.3. https://github.com/NCAR/Fields.
528 Open Source Geospatial Foundation. 2019. Geoserver: an open source software server for
529   sharing and editing geospatial data. GeoServer 2.17.1.
530   http://geoserver.org/release/stable/.
531 R Development Core Team. 2015. R: A language and environment for statistical computing. R
532   Foundation for Statistical Computing. Vienna, Austria.
533 Rolland C. 2003. Spatial and Seasonal Variations of Air Temperature Lapse Rates in Alpine
534   Regions. *Journal of Climate* 16:1032-1046. 10.1175/1520-
535   0442(2003)016<1032:sasvoa>2.0.co;2
536 Sobrino J, Julien Y, and García-Monteiro S. 2020. Surface Temperature of the Planet Earth
537   from Satellite Data. *Remote Sensing* 12:218. 10.3390/rs12020218
538 Su CH, Eizenberg N, Steinle P, Jakob D, Fox-Hughes P, White CJ, Rennie S, Franklin C,
539   Dharssi I, and Zhu H. 2019. BARRA v1.0: the Bureau of Meteorology Atmospheric high-
540   resolution Regional Reanalysis for Australia. *Geosci Model Dev* 12:2049-2068.
541   10.5194/gmd-12-2049-2019
542 Trewin BC. 2005. A notable frost hollow at Coonabarabran, New South Wales. *Australian*
543   *Meteorological Magazine* 54:15-21.
544 Wang K, Sun J, Cheng G, and Jiang H. 2011. Effect of altitude and latitude on surface air
545   temperature across the Qinghai-Tibet Plateau. *Journal of Mountain Science* 8:808-816.
546   10.1007/s11629-011-1090-2
547 Webb M, Hall A, Kidd D, and Minasny B. 2016. Local-scale spatial modelling for interpolating
548   climatic temperature variables to predict agricultural plant suitability. *Theoretical and*
549   *Applied Climatology* 124:1145-1165. 10.1007/s00704-015-1461-7
550 Webb MA, Kidd D, and Minasny B. 2020. Near real-time mapping of air temperature at high
551   spatiotemporal resolutions in Tasmania, Australia. *Theoretical and Applied Climatology*
552   141:1181-1201. 10.1007/s00704-020-03259-4
553 Williams M, Cornford D, Bastin L, Jones R, and Parker S. 2011. Automatic processing, quality
554   assurance and serving of real-time weather data. *Computers & Geosciences* 37:353-
555   362. https://doi.org/10.1016/j.cageo.2010.05.010
556 Xu Y, Knudby A, Shen Y, and Liu Y. 2018. Mapping Monthly Air Temperature in the Tibetan
557   Plateau From MODIS Data Based on Machine Learning Methods. *IEEE Journal of*
558   *Selected Topics in Applied Earth Observations and Remote Sensing* 11:345-354.
559   10.1109/JSTARS.2017.2787191
560 Xue W, Guo J, Zhang Y, Zhou S, Wang Y, Miao Y, Liu L, Xu H, Li J, Chen D, and Liu H. 2019.
561   Declining diurnal temperature range in the North China Plain related to environmental
562   changes. *Climate Dynamics* 52:6109-6119. 10.1007/s00382-018-4505-8
563

Figure 1

Workflow developed for this study
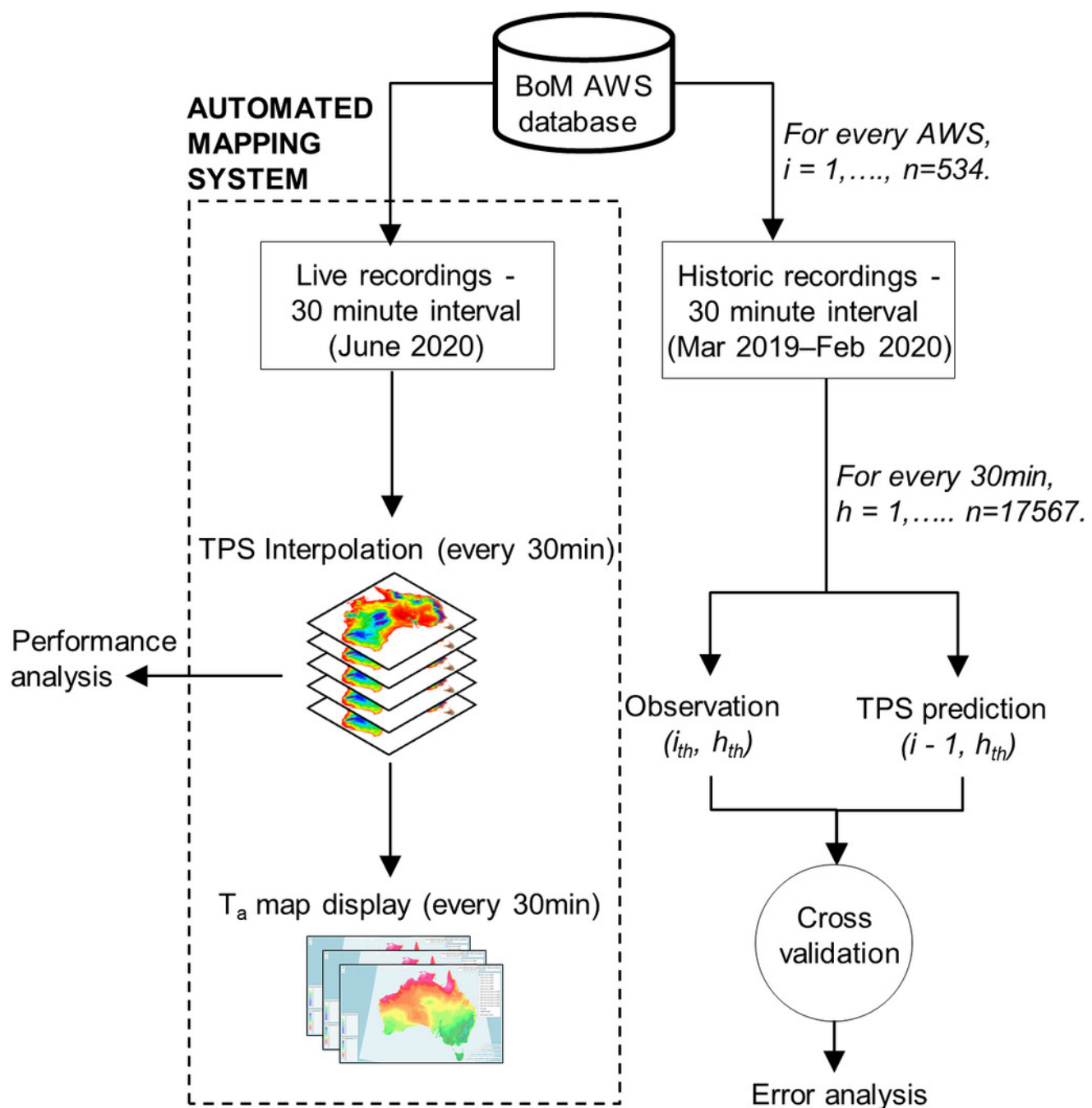
Figure 2

Elevation map of Australia with locations of major towns/cities and Bureau of Meteorology (BoM) automatic weather stations (AWS).

Purple dots illustrate AWS locations. Red dots denote locations of notable AWS sites (refer results section)
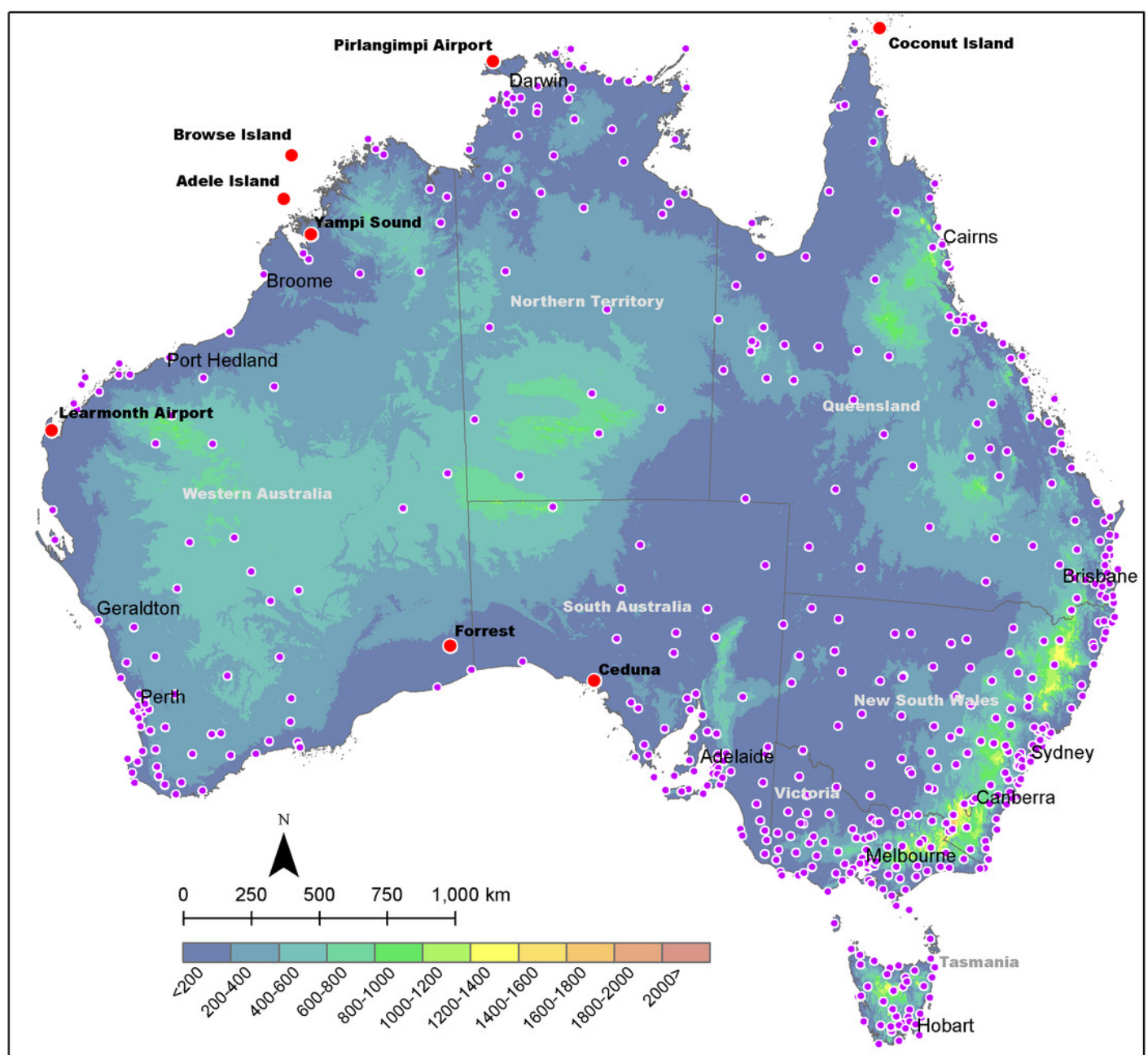
Figure 3

Histogram plots of validation metrics for MAE, RMSE, R^2 and P_c according to each season.

(A) MAE in autumn. (B) MAE in winter. (C) MAE in spring. (D) MAE in summer. (E) RMSE in autumn. (F) RMSE in winter. (G) RMSE in spring. (H) RMSE in summer. (I) R^2 in autumn. (J) R^2 in winter. (K) R^2 in spring. (L) R^2 in summer. (M) P_c in autumn. (N) P_c in winter. (O) P_c in spring. (P) P_c in summer.
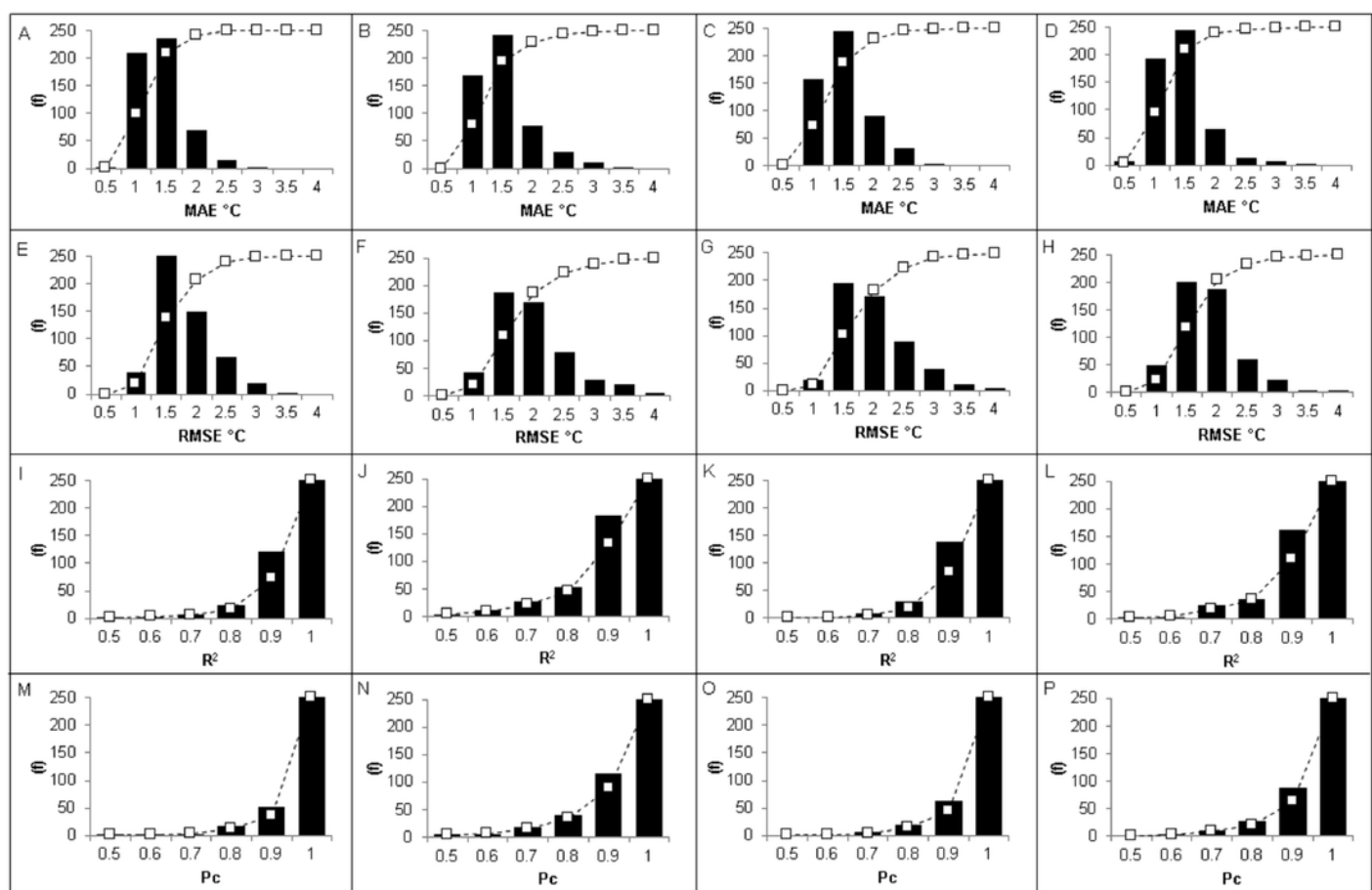
Figure 4

Interpolated validation metrics (using a two-dimensional smoothing spline) for MAE, RMSE, R^2 and P_c according to each season.

(A) MAE in autumn. (B) MAE in winter. (C) MAE in spring. (D) MAE in summer. (E) RMSE in autumn. (F) RMSE in winter. (G) RMSE in spring. (H) RMSE in summer. (I) R^2 in autumn. (J) R^2 in winter. (K) R^2 in spring. (L) R^2 in summer. (M) P_c in autumn. (N) P_c in winter. (O) P_c in spring. (P) P_c in summer. Black dots within each panel denote AWS sites where values are above the 95th percentile (labelled with their corresponding value).
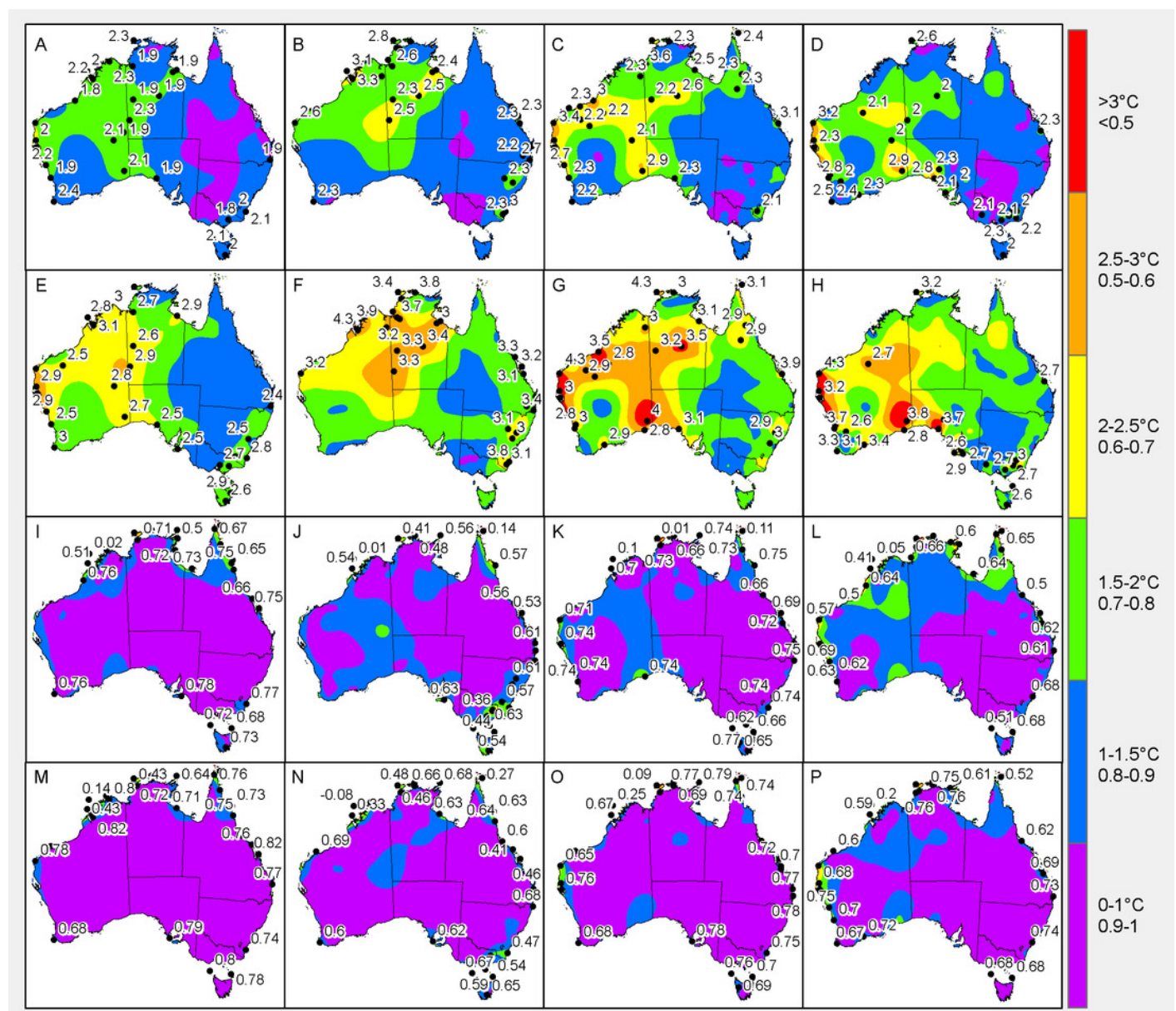
Figure 5

Interpolated MAE values (using a two-dimensional smoothing spline) according to each season and time of day.

(A) autumn, 12 am. (B) autumn, 3 am. (C) autumn, 6 am. (D) autumn, 9 am. (E) autumn, 12 pm. (F) autumn, 3 pm. (G) autumn, 6 pm. (H) autumn, 9 pm. (I) winter, 12 am. (J) winter, 3 am. (K) winter, 6 am. (L) winter, 9 am. (M) winter, 12 pm. (N) winter, 3 pm. (O) winter, 6 pm. (P) winter, 9 pm. (Q) spring, 12 am. (R) spring, 3 am. (S) spring, 6 am. (T) spring, 9 am. (U) spring, 12 pm. (V) spring, 3 pm. (W) spring, 6 pm. (X) spring, 9 pm. (Y) summer, 12 am. (Z) summer, 3 am. (AA) summer, 6 am. (BB) summer, 9 am. (CC) summer, 12 pm. (DD) summer, 3 pm. (EE) summer, 6 pm. (FF) summer, 9 pm.
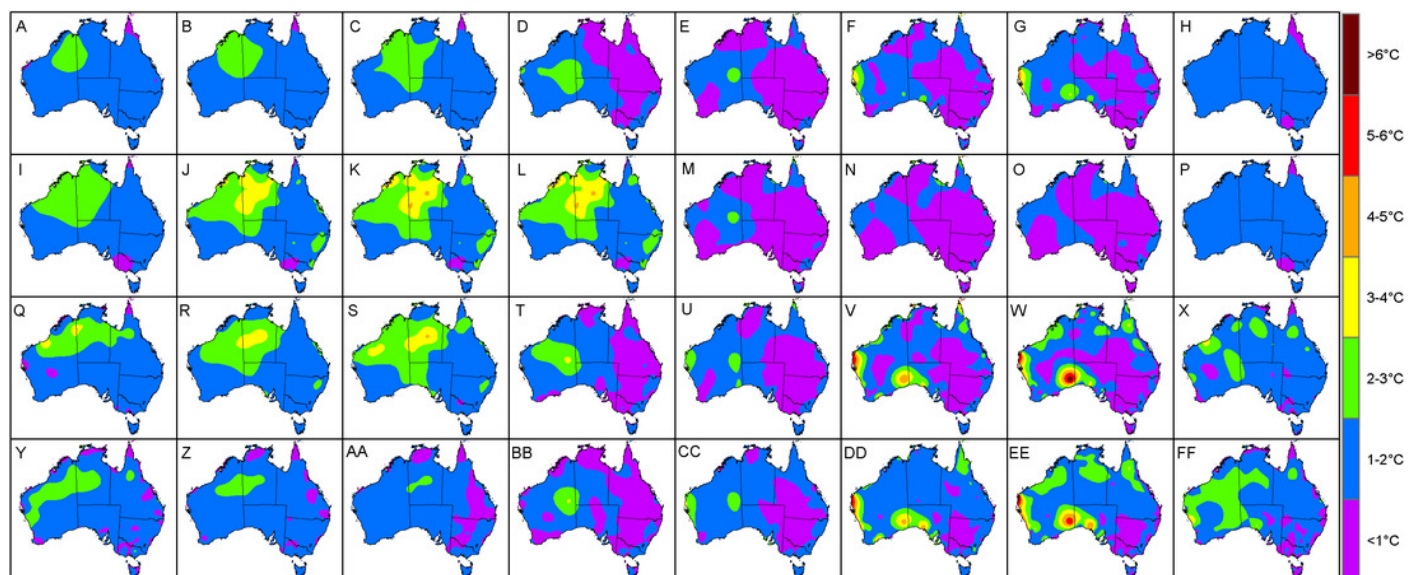
Figure 6

Interpolated RMSE values (using a two-dimensional smoothing spline) according to each season and time of day.

(A) autumn, 12 am. (B) autumn, 3 am. (C) autumn, 6 am. (D) autumn, 9 am. (E) autumn, 12 pm. (F) autumn, 3 pm. (G) autumn, 6 pm. (H) autumn, 9 pm. (I) winter, 12 am. (J) winter, 3 am. (K) winter, 6 am. (L) winter, 9 am. (M) winter, 12 pm. (N) winter, 3 pm. (O) winter, 6 pm. (P) winter, 9 pm. (Q) spring, 12 am. (R) spring, 3 am. (S) spring, 6 am. (T) spring, 9 am. (U) spring, 12 pm. (V) spring, 3 pm. (W) spring, 6 pm. (X) spring, 9 pm. (Y) summer, 12 am. (Z) summer, 3 am. (AA) summer, 6 am. (BB) summer, 9 am. (CC) summer, 12 pm. (DD) summer, 3 pm. (EE) summer, 6 pm. (FF) summer, 9 pm.
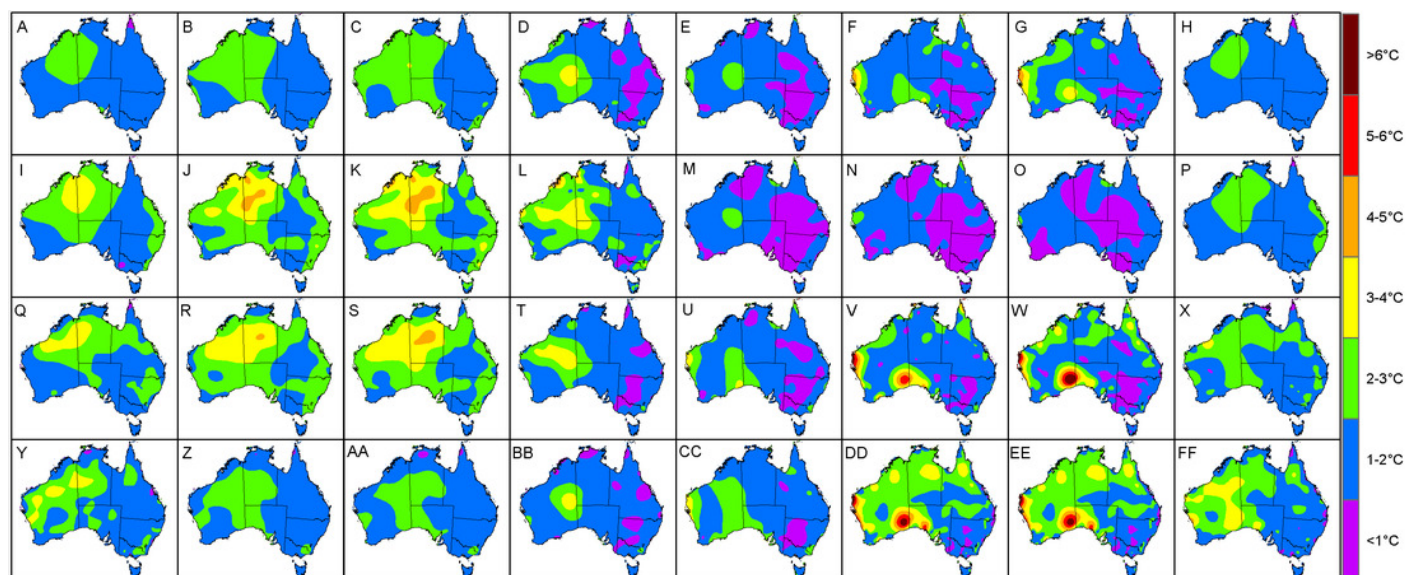
Figure 7

Line plots for selected AWS sites over a 24-hour period in each season for validation metrics concerning MAE, RMSE, R^2 and P_c.

(A) MAE in autumn. (B) MAE in winter. (C) MAE in spring. (D) MAE in summer. (E) RMSE in autumn. (F) RMSE in winter. (G) RMSE in spring. (H) RMSE in summer. (I) R^2 in autumn. (J) R^2 in winter. (K) R^2 in spring. (L) R^2 in summer. (M) P_c in autumn. (N) P_c in winter. (O) P_c in spring. (P) P_c in summer.
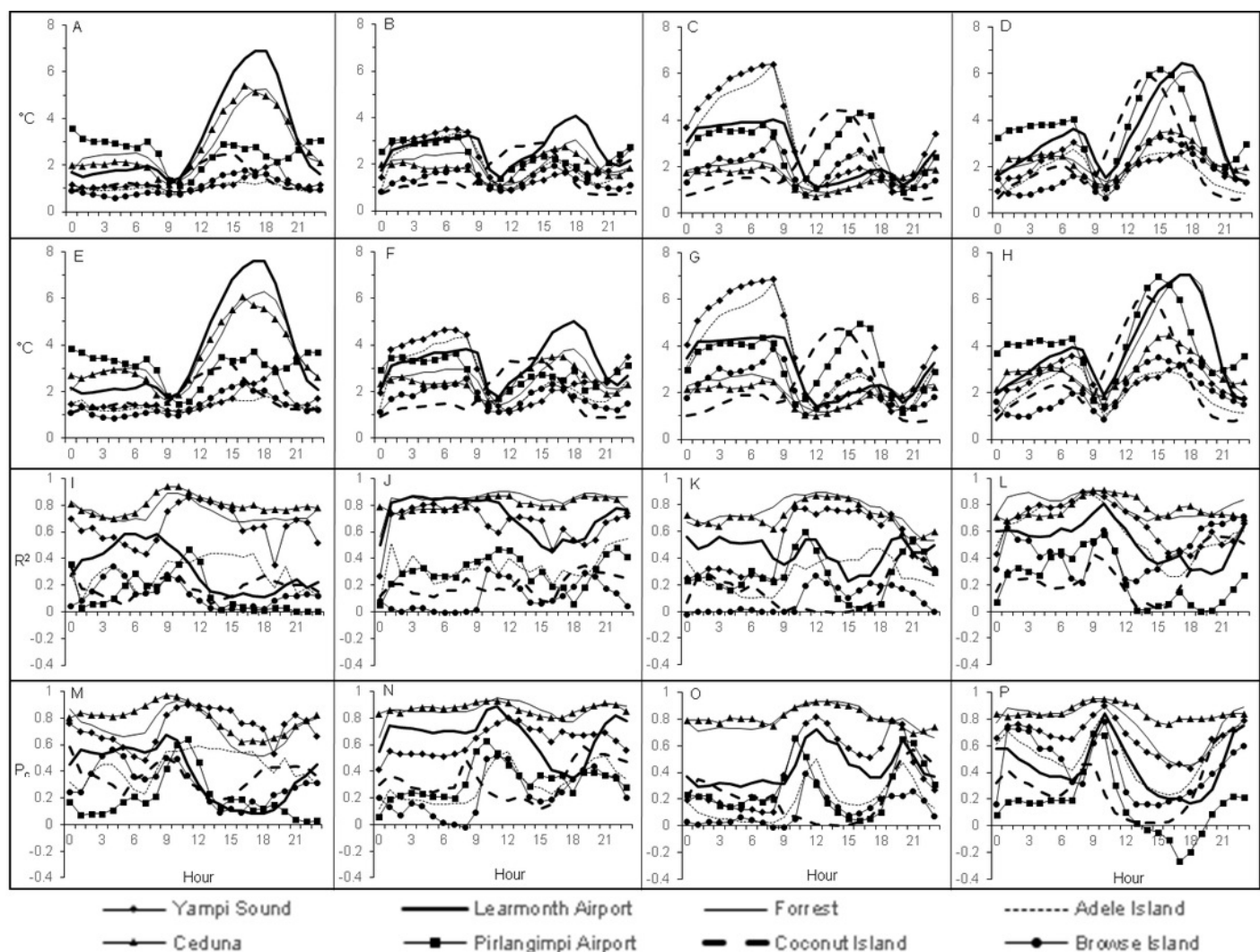
Figure 8

Interpolated R^2 values (using a two-dimensional smoothing spline) according to each season and time of day.

(A) autumn, 12 am. (B) autumn, 3 am. (C) autumn, 6 am. (D) autumn, 9 am. (E) autumn, 12 pm. (F) autumn, 3 pm. (G) autumn, 6 pm. (H) autumn, 9 pm. (I) winter, 12 am. (J) winter, 3 am. (K) winter, 6 am. (L) winter, 9 am. (M) winter, 12 pm. (N) winter, 3 pm. (O) winter, 6 pm. (P) winter, 9 pm. (Q) spring, 12 am. (R) spring, 3 am. (S) spring, 6 am. (T) spring, 9 am. (U) spring, 12 pm. (V) spring, 3 pm. (W) spring, 6 pm. (X) spring, 9 pm. (Y) summer, 12 am. (Z) summer, 3 am. (AA) summer, 6 am. (BB) summer, 9 am. (CC) summer, 12 pm. (DD) summer, 3 pm. (EE) summer, 6 pm. (FF) summer, 9 pm.
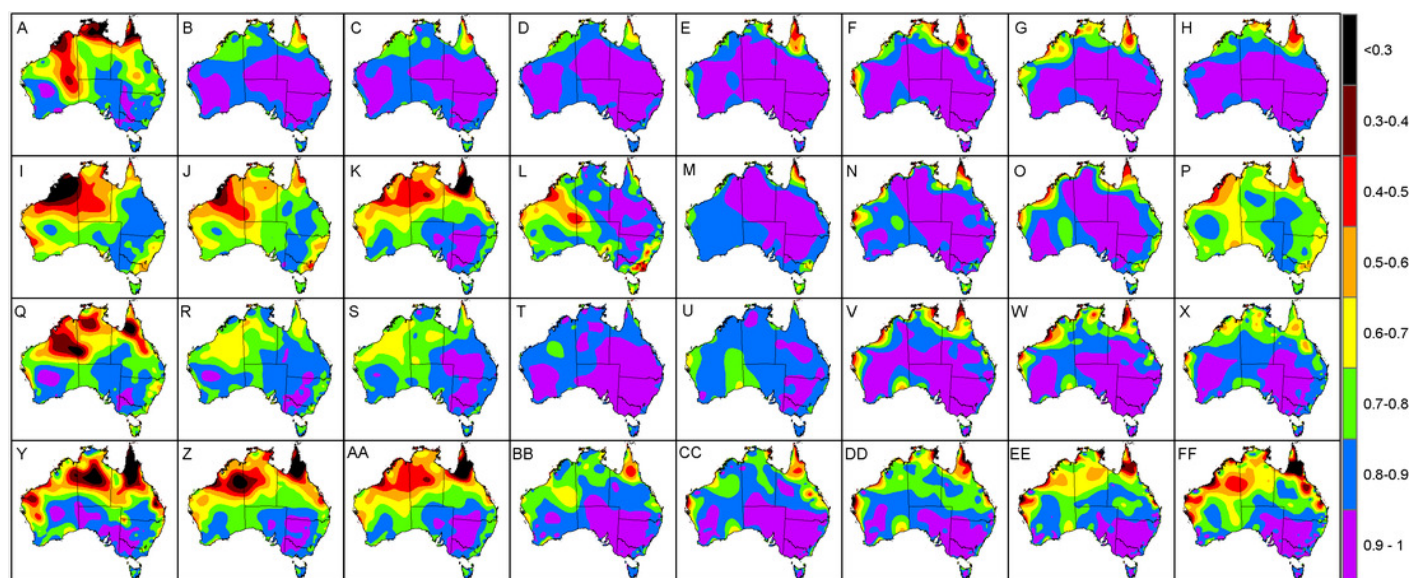
Figure 9

Interpolated P_c values (using a two-dimensional smoothing spline) according to each season and time of day.

(A) autumn, 12 am. (B) autumn, 3 am. (C) autumn, 6 am. (D) autumn, 9 am. (E) autumn, 12 pm. (F) autumn, 3 pm. (G) autumn, 6 pm. (H) autumn, 9 pm. (I) winter, 12 am. (J) winter, 3 am. (K) winter, 6 am. (L) winter, 9 am. (M) winter, 12 pm. (N) winter, 3 pm. (O) winter, 6 pm. (P) winter, 9 pm. (Q) spring, 12 am. (R) spring, 3 am. (S) spring, 6 am. (T) spring, 9 am. (U) spring, 12 pm. (V) spring, 3 pm. (W) spring, 6 pm. (X) spring, 9 pm. (Y) summer, 12 am. (Z) summer, 3 am. (AA) summer, 6 am. (BB) summer, 9 am. (CC) summer, 12 pm. (DD) summer, 3 pm. (EE) summer, 6 pm. (FF) summer, 9 pm.
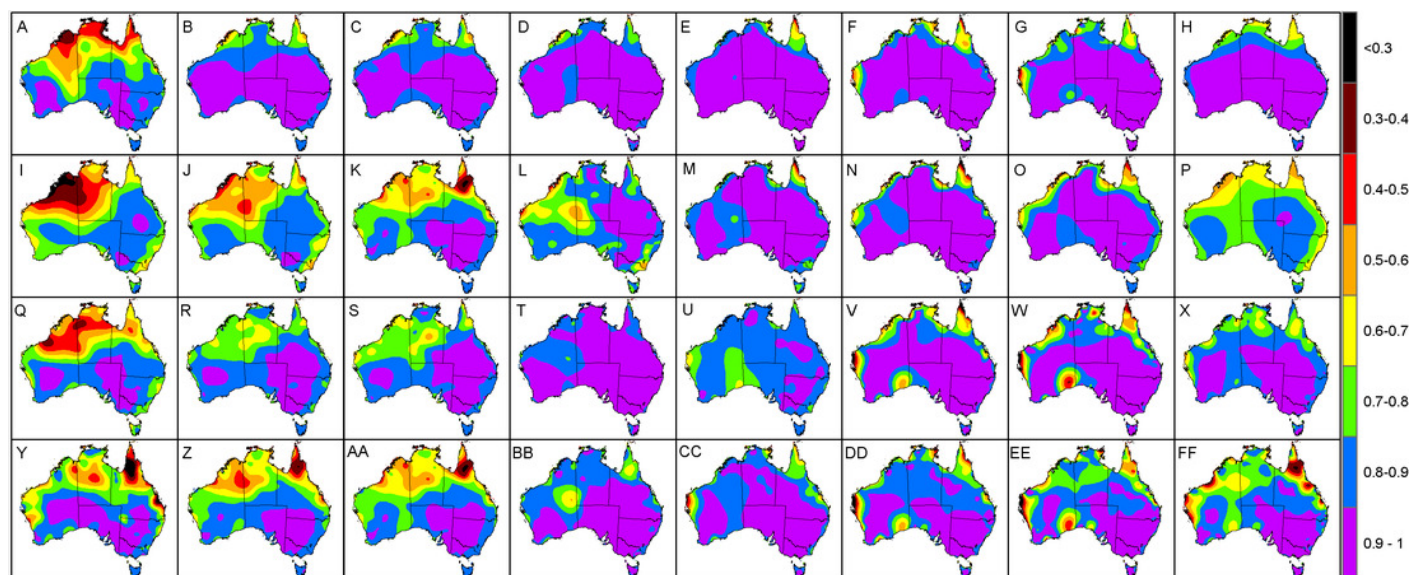
Figure 10

Frequency of map completion times (minutes from AWS observation time, T) in accordance to their bi-hourly processing intervals.

(A) 0 minutes. (B) 30 minutes.
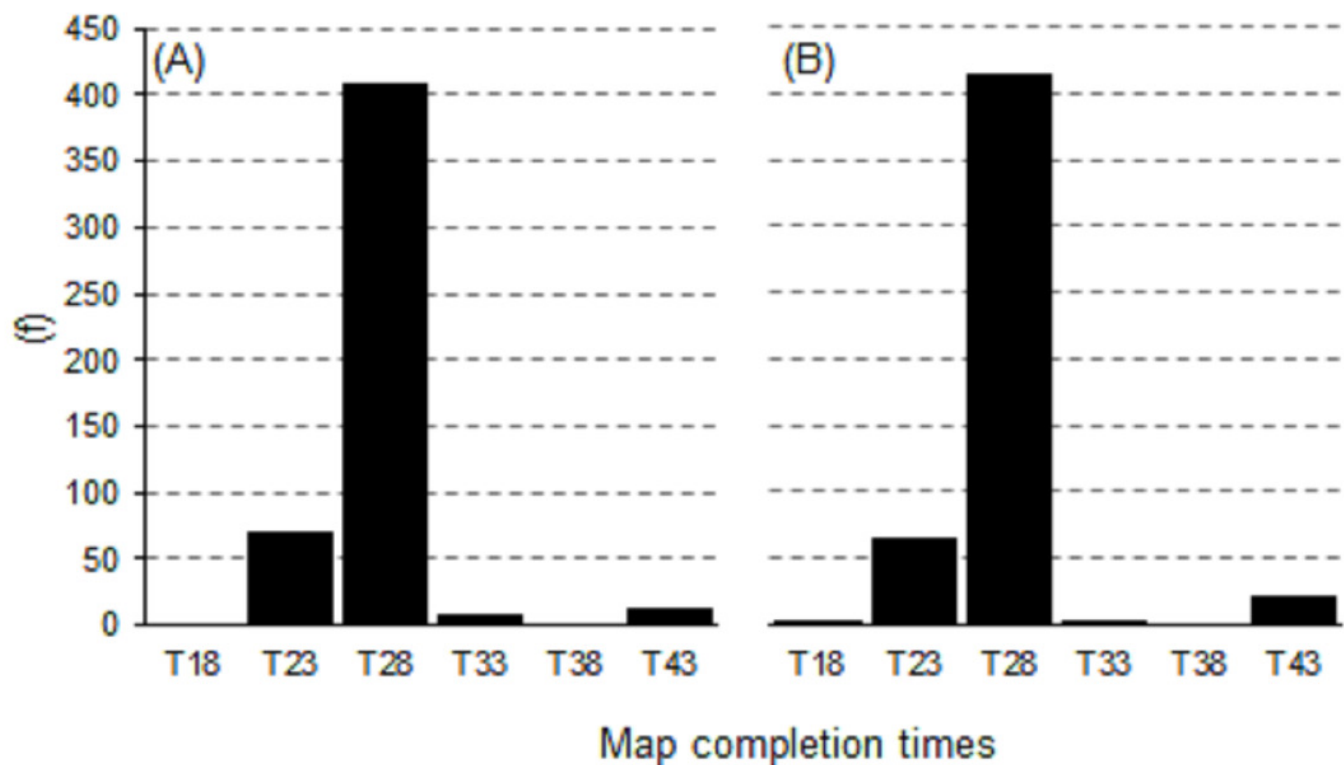
Figure 11

Box and whisker plots for AWS import times (minutes from AWS observation time, T) in accordance to their bi-hourly processing intervals.

(A) 0 minutes. (B) 30 minutes. Numbers in bold denote frequencies when the 480-observation threshold limit was reached.
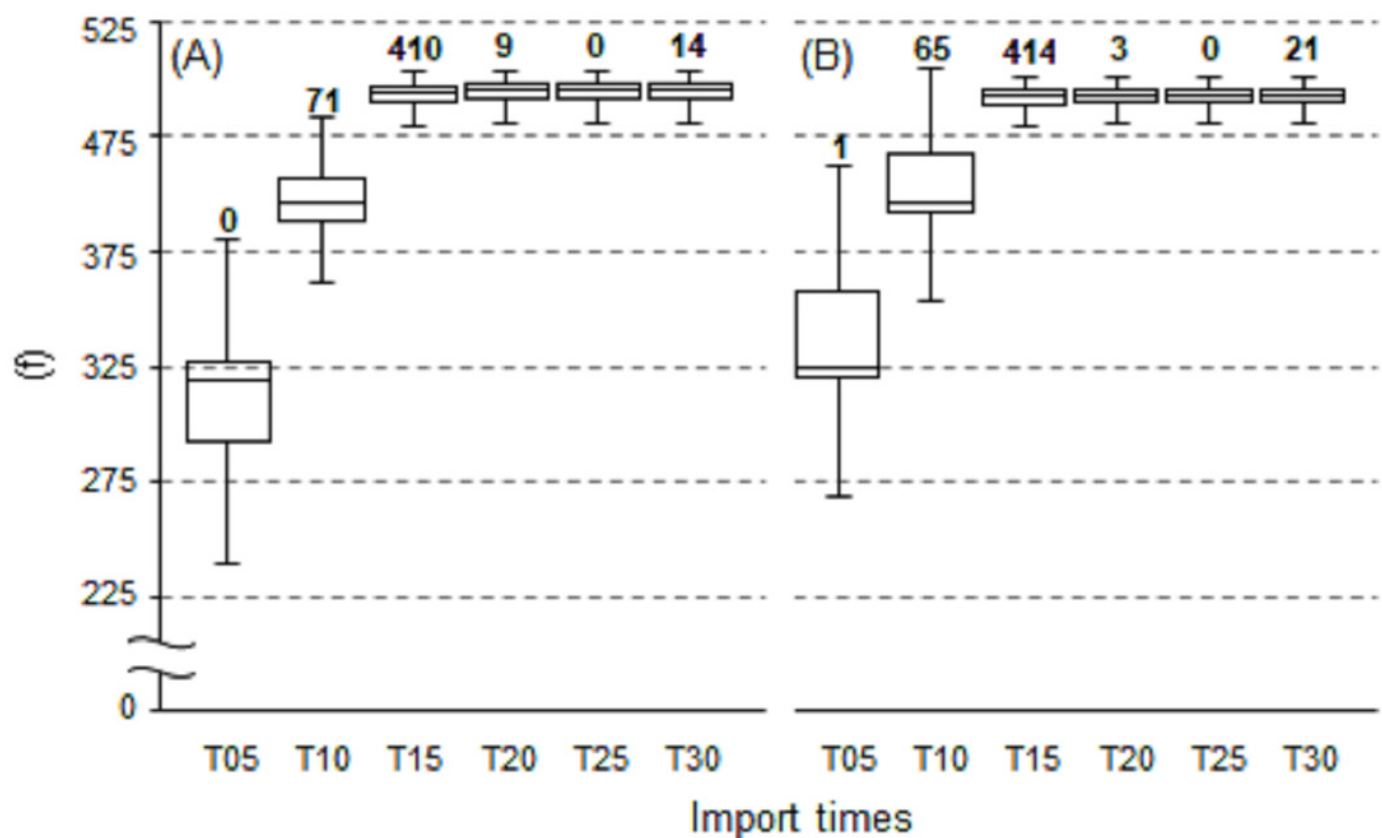
Figure 12

Web map environment for displaying and spatially interrogating the near real-time T_a outputs. An example can be viewed at URL http://austemperature.live/.

© OpenStreetMap contributors, CC BY SA
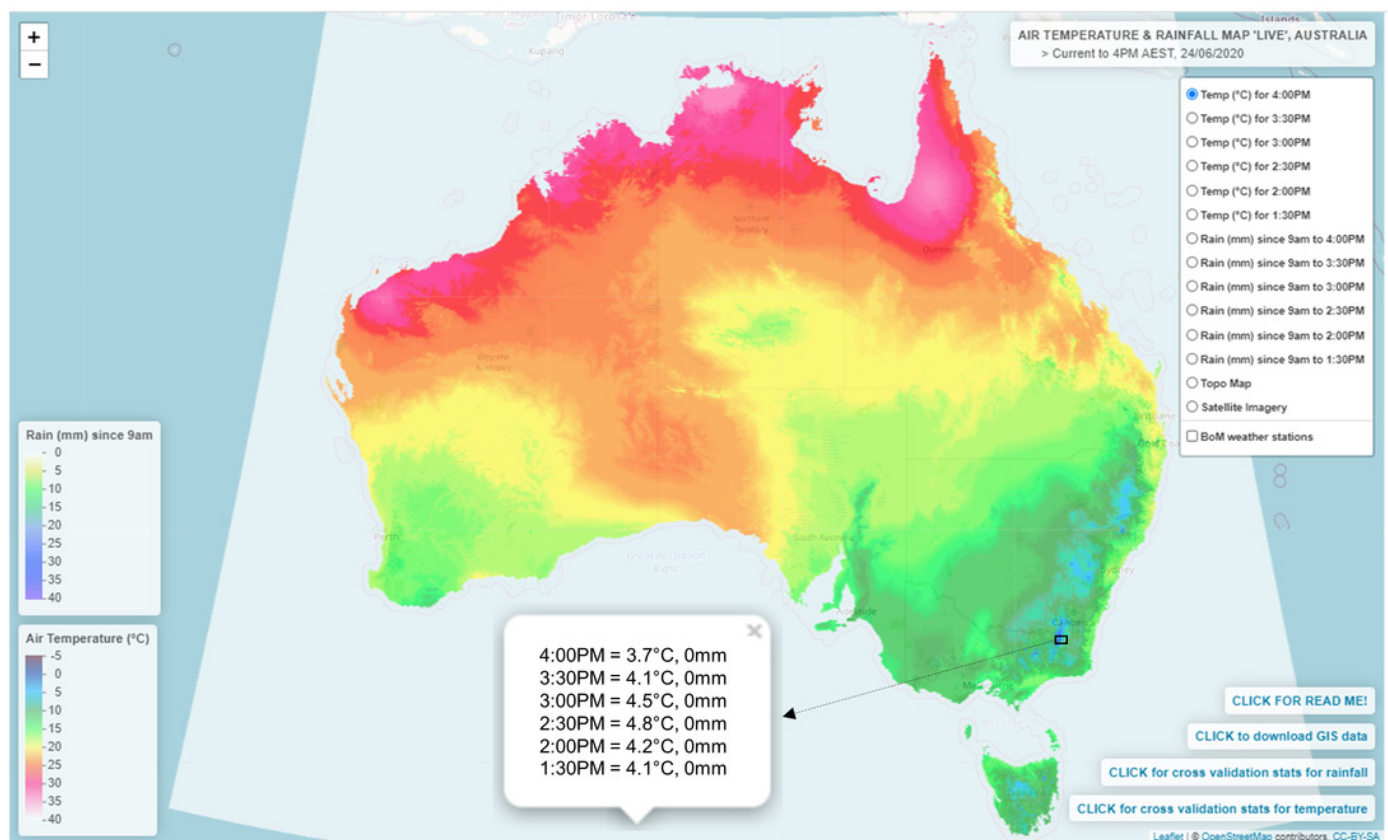
Validation statistics for the TPS interpolation procedure showing R^2, P_c, MAE (°C) and RMSE (°C) values - averaged for each AWS site according to the season.

sd standard deviation, min minimum, max maximum

	Summer	Autumn	Winter	Spring
R^2				
mean	0.89	0.91	0.86	0.91
min	0.05	0.02	0.01	0.01
max	0.99	0.99	0.97	0.99
sd	0.11	0.09	0.11	0.09
P_c				
mean	0.92	0.94	0.92	0.93
min	0.18	0.14	0.18	0.09
max	0.99	0.99	0.99	0.99
sd	0.09	0.08	0.09	0.08
MAE				
mean	1.2	1.2	1.3	1.3
min	0.5	0.5	0.5	0.6
max	3.2	2.8	3.3	3.6
sd	0.4	0.4	0.5	0.5
RMSE				
mean	1.6	1.6	1.7	1.7
min	0.6	0.7	0.7	0.8
max	4.3	3.5	4.3	4.3
sd	0.5	0.5	0.6	0.6

K-fold cross-validation statistics for the TPS interpolation procedure showing R^2, P_c, MAE (°C) and RMSE (°C) values - averaged for each season.

sd standard deviation, min minimum, max maximum

	Summer	Autumn	Winter	Spring
R^2				
mean	0.93	0.92	0.9	0.92
min	0.4	0.43	0.04	0.41
max	0.99	0.99	0.99	0.99
sd	0.04	0.05	0.07	0.06
P_c				
mean	0.96	0.96	0.95	0.96
min	0.62	0.62	0.19	0.63
max	1	1	1	1
sd	0.02	0.03	0.04	0.03
MAE				
mean	1.2	1.2	1.3	1.3
min	0.5	0.5	0.4	0.5
max	2.7	2.5	3	3.1
sd	0.3	0.3	0.4	0.4
RMSE				
mean	1.7	1.6	1.7	1.8
min	0.7	0.6	0.5	0.7
max	6.4	7.6	10	7.4
sd	0.4	0.4	0.6	0.5